



HAL
open science

A MeerKAT, e-MERLIN, H.E.S.S. and Swift search for persistent and transient emission associated with three localised FRBs

J. O. Chibueze, M. Caleb, L. Spitler, H. Ashkar, F. Schüssler, B. W. Stappers, C. Venter, I. Heywood, A. M. S. Richards, D. R. A. Williams, et al.

► **To cite this version:**

J. O. Chibueze, M. Caleb, L. Spitler, H. Ashkar, F. Schüssler, et al.. A MeerKAT, e-MERLIN, H.E.S.S. and Swift search for persistent and transient emission associated with three localised FRBs. Monthly Notices of the Royal Astronomical Society, 2022, 515 (1), pp.1365-1379. 10.1093/mnras/stac1601 . insu-03713226

HAL Id: insu-03713226

<https://insu.hal.science/insu-03713226>

Submitted on 13 Apr 2023

HAL is a multi-disciplinary open access archive for the deposit and dissemination of scientific research documents, whether they are published or not. The documents may come from teaching and research institutions in France or abroad, or from public or private research centers.

L'archive ouverte pluridisciplinaire **HAL**, est destinée au dépôt et à la diffusion de documents scientifiques de niveau recherche, publiés ou non, émanant des établissements d'enseignement et de recherche français ou étrangers, des laboratoires publics ou privés.

A MeerKAT, e-MERLIN, H.E.S.S., and *Swift* search for persistent and transient emission associated with three localized FRBs

J. O. Chibueze^{1b, 1,2*} M. Caleb^{1b, 3,4*} L. Spitler^{1b, 5} H. Ashkar,^{6,7} F. Schüssler,⁶ B. W. Stappers^{1b, 4} C. Venter,¹ I. Heywood,^{8,9,10} A. M. S. Richards,³ D. R. A. Williams,³ M. Kramer,^{3,5} R. Beswick,³ M. C. Bezuidenhout,³ R. P. Breton,³ L. N. Driessen,¹¹ F. Jankowski,³ E. F. Keane,¹² M. Malenta,³ M. Mickaliger,³ V. Morello,³ H. Qiu,¹³ K. Rajwade,³ S. Sanidas,³ M. Surnis,³ T. W. Scragg,³ C. R. H. Walker,⁵ N. Wrigley,³ H.E.S.S. Collaboration: F. Aharonian,^{14,15,16} F. Ait Benkhali,¹⁷ E. O. Angüner,¹⁸ M. Backes,^{1,19} V. Baghmanyan,²⁰ V. Barbosa Martins,²¹ R. Batzofin,²² Y. Becherini,^{23,24} D. Berge,²¹ M. Böttcher,¹ C. Boisson,²⁵ J. Bolmont,²⁶ M. de Bony de Lavergne,²⁷ M. Breuhaus,¹⁵ R. Brose,¹⁴ F. Brun,⁶ T. Bulik,²⁸ F. Cangemi,²⁶ S. Caroff,²⁶ S. Casanova,²⁰ J. Catalano,²⁹ M. Cerruti,²³ T. Chand,¹ A. Chen,²² O. U. Chibueze,¹ G. Cotter,³⁰ P. Cristofari,²⁵ J. Damascene Mbarubucyeye,²¹ J. Devin,³¹ A. Djannati-Ataï,²³ A. Dmytriiev,¹ K. Egberts,³² J.-P. Ernenwein,¹⁸ A. Fiasson,²⁷ G. Fichet de Clairfontaine,²⁵ G. Fontaine,⁷ S. Funk,²⁹ S. Gabici,²³ S. Ghafourizadeh,¹⁷ G. Giavitto,²¹ D. Glawion,²⁹ M.-H. Grondin,³¹ M. Hörbe,³⁰ C. Hoischen,³² T. L. Holch,²¹ Zhiqiu Huang,¹⁵ M. Jamrozy,³³ F. Jankowsky,¹⁷ V. Joshi,²⁹ I. Jung-Richardt,²⁹ E. Kasai,¹⁹ K. Katarzyński,³⁴ U. Katz,²⁹ B. Khélifi,²³ W. Kluźniak,³⁵ Nu. Komin,²² K. Kosack,⁶ D. Kostunin,²¹ A. Lemièrre,²³ J.-P. Lenain,²⁶ F. Leuschner,³⁶ T. Lohse,³⁷ A. Luashvili,²⁵ I. Lypova,¹⁷ J. Mackey,¹⁴ D. Malyshev,³⁶ V. Marandon,¹⁵ P. Marchegiani,²² A. Marcowith,³⁸ G. Martí-Devesa,³⁹ R. Marx,¹⁷ A. Mitchell,^{15,29} R. Moderski,³⁵ L. Mohrmann,¹⁵ E. Moulin,⁶ J. Muller,⁷ K. Nakashima,²⁹ M. de Naurois,⁷ A. Nayerhoda,²⁰ J. Niemiec,²⁰ A. Priyana Noel,³³ P. O'Brien,⁴⁰ S. Ohm,²¹ L. Olivera-Nieto,¹⁵ E. de Ona Wilhelmi,²¹ M. Ostrowski,³³ S. Panny,³⁹ R. D. Parsons,³⁷ S. Pita,²³ V. Poireau,²⁷ D. A. Prokhorov,⁴¹ H. Prokoph,²¹ G. Pühlhofer,³⁶ A. Quirrenbach,¹⁷ P. Reichherzer,⁶ A. Reimer,³⁹ O. Reimer,³⁹ G. Rowell,⁴² B. Rudak,³⁵ E. Ruiz-Velasco,¹⁵ V. Sahakian,⁴³ S. Sailer,¹⁵ H. Salzmann,³⁶ D. A. Sanchez,²⁷ A. Santangelo,³⁶ M. Sasaki,²⁹ H. M. Schutte,¹ U. Schwanke,³⁷ J. N. S. Shapopi,¹⁹ A. Specovius,²⁹ S. Spencer,³⁰ R. Steenkamp,¹⁹ S. Steinmassl,¹⁵ T. Takahashi,⁴⁴ T. Tanaka,⁴⁵ C. Thorpe-Morgan,³⁶ N. Tsuji,⁴⁶ C. van Eldik,²⁹ J. Veh,²⁹ J. Vink,⁴¹ S. J. Wagner,¹⁷ A. Wiercholska,²⁰ Yu Wun Wong,²⁹ A. Yusufzai,²⁹ M. Zacharias,^{1,25} D. Zargaryan,^{14,16} A. A. Zdziarski,³⁵ A. Zech,²⁵ S. J. Zhu,²¹ S. Zouari,²³ and N. Żywucka¹

Affiliations are listed at the end of the paper

Accepted 2022 June 6. Received 2022 June 6; in original form 2022 January 5

ABSTRACT

We report on a search for persistent radio emission from the one-off fast radio burst (FRB) 20190714A, as well as from two repeating FRBs, 20190711A and 20171019A, using the MeerKAT radio telescope. For FRB 20171019A, we also conducted simultaneous observations with the High-Energy Stereoscopic System (H.E.S.S.) in very high-energy gamma rays and searched for signals in the ultraviolet, optical, and X-ray bands. For this FRB, we obtain a UV flux upper limit of $1.39 \times 10^{-16} \text{ erg cm}^{-2} \text{ s}^{-1} \text{ \AA}^{-1}$, X-ray limit of $\sim 6.6 \times 10^{-14} \text{ erg cm}^{-2} \text{ s}^{-1}$ and a limit on the very high energy gamma-ray flux $\Phi(E > 120 \text{ GeV}) < 1.7 \times 10^{-12} \text{ erg cm}^{-2} \text{ s}^{-1}$. We obtain a radio upper limit of $\sim 15 \mu\text{Jy beam}^{-1}$ for persistent emission at the locations of both FRBs 20190711A and 20171019A with MeerKAT. However, we detected an almost unresolved (ratio of integrated flux to peak flux is ~ 1.7 beam) radio emission, where the synthesized beam size was ~ 8 arcsec size with a peak brightness of $\sim 53 \mu\text{Jy beam}^{-1}$ at MeerKAT and $\sim 86 \mu\text{Jy beam}^{-1}$ at e-MERLIN, possibly associated with FRB 20190714A at $z = 0.2365$. This represents the first detection of persistent continuum radio emission potentially associated with a (as-yet) non-

* E-mail: james.chibueze@gmail.com (JC); manishacaleb@gmail.com (MC)

repeating FRB. If the association is confirmed, one of the strongest remaining distinction between repeaters and non-repeaters would no longer be applicable. A parallel search for repeat bursts from these FRBs revealed no new detections down to a fluence of 0.08 Jy ms for a 1 ms duration burst.

Key words: radiation mechanisms: non-thermal – radio continuum: galaxies – (*transients:*) fast radio burst.

1 INTRODUCTION

Fast radio bursts (FRBs) are luminous transients that last for microseconds to milliseconds and occur at extragalactic to cosmological distances (e.g. Lorimer et al. 2007; Thornton et al. 2013; Macquart et al. 2020). The estimated high radio luminosities and associated brightness temperatures required to produce these short-timescale energetic events at such distances are what makes them intriguing (Caleb & Keane 2021; Petroff, Hessels & Lorimer 2022). They have been observed to emit from ~ 110 MHz – 8 GHz, though not yet across a wide and continuous frequency band due to the variable band-limited spectra of the single pulses. Over 600 FRBs have been reported¹ of which ~ 20 have been seen to repeat, and it is presently uncertain whether they all do (Caleb et al. 2019; James et al. 2020). The extraordinary observed characteristics of the repeating and non-repeating FRBs have led to various progenitor models with the bulk of them favouring neutron stars. Progenitor theories include binary neutron star mergers and collisions (Totani 2013; Yamasaki, Totani & Kiuchi 2018), giant pulses from extragalactic pulsars (Cordes & Wasserman 2016; Popov & Pshirkov 2016), hyperflares, and giant flares from magnetars (Popov & Postnov 2013; Popov, Postnov & Pshirkov 2018), binary white dwarf mergers (Kashiyama, Ioka & Mészáros 2013), neutron star ‘combing’ (Zhang 2018) and interactions of neutron stars with active galactic nuclei (Vieyro et al. 2017) [see Platts et al. (2019) for a list of potential progenitors]. Some of these models predict radio afterglows accompanying an FRB with time-scales of days to years. Liu et al. (2016) propose that the merger of a Kerr–Newman black hole binary is one of the plausible central engines for FRBs and their afterglows. Dai, Wang & Yu (2017), however, suggest that the persistent emission is due to an ultra-relativistic pulsar wind nebula sweeping up its ambient medium with FRBs repeatedly produced through one of several potential mechanisms. In the magnetar model by Metzger, Berger & Margalit (2017) and Margalit, Berger & Metzger (2019), FRBs produced by binary neutron star mergers and accretion induced collapse are expected to be accompanied by persistent radio continuum emission on timescales of months to years. The persistent emission is powered by the nebula of relativistic electrons and magnetic fields inflated by the magnetar flares (Margalit et al. 2019). The existence of persistent emission associated with FRBs could provide vital clues to their origin. Moreover, potential candidates and models for FRB progenitors predict counterparts in the X-ray and TeV bands. For example, a model by Lyubarsky (2014) predicts millisecond outbursts of TeV emission accompanying FRBs from magnetars. In 2020, FRB 20200428 was discovered for the first time from a galactic magnetar, SGR 1935 + 2154. Furthermore, an X-ray counterpart to this FRB was detected for the first time by several instruments (Insight-HXMT 2020; Mereghetti et al. 2020; Ridnaia et al. 2021; Tavani et al. 2021).

Of the 20 FRBs that have been associated with host galaxies² (Niu et al. 2022), the subarcsecond localization of the first repeating FRB 20121102A to a host galaxy at a redshift of $z = 0.19273 \pm 0.0008$

(Bassa et al. 2017; Chatterjee et al. 2017; Tendulkar et al. 2017a) showed that it is physically associated with a compact ($\lesssim 0.2$ mas angular extent at 5.0 GHz), persistent radio source of luminosity $\nu L_\nu \sim 10^{39}$ erg s⁻¹ at a few GHz (Chatterjee et al. 2017; Marcote et al. 2017). This source is detectable from 300 MHz to 26 GHz (Chatterjee et al. 2017; Resmi, Vink & Ishwara-Chandra 2021) and is seen to exhibit ~ 10 per cent variability on day time-scales. In contrast, a similar submilliarcsecond localization of another repeating FRB 20180916B to a nearby massive spiral galaxy at $z = 0.0337 \pm 0.0002$ (Marcote et al. 2020) showed no associated persistent radio emission. This places a strong upper limit on the persistent source luminosity of $\nu L_\nu \lesssim 7.6 \times 10^{35}$ erg s⁻¹ at 1.6 GHz, which is three orders of magnitude lower than that of FRB 20121102A. Recently, the CHIME/FRB collaboration announced heightened activity in the repeating FRB 20201124A (Chime/FRB Collaboration 2021), which was localized to a host galaxy at a redshift of $z = 0.0979 \pm 0.0001$ (Fong et al. 2021; Ravi et al. 2022). Persistent radio emission was detected by the upgraded Giant Metrewave Radio Telescope (uGMRT) (Wharton et al. 2021) and the Karl G. Jansky Very Large Array (VLA; Ricci et al. 2021) on angular scales of a few arcseconds. The emission was however resolved out on scales of ~ 0.1 arcsec with the European VLBI Network (Marcote et al. 2021) indicating that it was not compact, and consequently different from that associated with FRBs 20121102A. More recently, a second repeating FRB, FRB 20190520B is seen to have similar characteristics to FRB 20211102A in terms of host galaxy properties, burst activity and association with a persistent radio source (Niu et al. 2022). This suggests that such persistent emission may be present in at least some FRBs and may play a vital role in their evolution (Law, Connor & Aggarwal 2022).

Localizations of four one-off FRBs through imaging of buffered raw voltage data at 1.4 GHz (Bannister et al. 2019; Prochaska et al. 2019; Macquart et al. 2020) by the Australian SKA Pathfinder (ASKAP) telescope resulted in non-detection of persistent radio continuum emission from the host galaxies (Bhandari et al. 2020). Australian Telescope Compact Array (ATCA) observations of FRBs 20180924B, 20181112A, 20190102C and 20190608B were conducted at a centre frequency of 6.5 GHz. No persistent emission as luminous as the one associated with FRB 20121102A was detected for the ASKAP FRBs (Bhandari et al. 2020). While the true age of FRB 20121102A is unknown, models based on polarization studies predict the age to be $\sim 6 - 17$ years (Hilmarsson et al. 2021). It is possible that younger, more active FRBs like FRB 20121102A and FRB 20190520B are associated with compact persistent radio emission while the emission might have faded over time for the older ones. The possibility of repeating FRBs not being so uncommon after all (Ravi 2019) along with the increasing arcsecond localizations of FRB from radio interferometers suggests that we are entering an era where we can begin to look for evidence of multiple classes by studying FRB host galaxies and multiwavelength counterparts.

In this paper, we report on the search for persistent radio emission in the host galaxies of one apparent one-off source (FRB 20190714A) and two repeating sources (FRBs 20171019A and 20190711A) (Kumar et al. 2019, 2021) using MeerKAT. In case of the latter, we also conducted simultaneous observations with the High Energy Stereoscopic System (H.E.S.S.) in very high-energy gamma-rays.

¹<https://www.wis-tns.org/>

²<https://frbhosts.org/>

Table 1. Details of the FRB fields observed with MeerKAT.

Field name	Observation date	Synthesized beam	rms ($\mu\text{Jy beam}^{-1}$)	Detected?
FRB 20171019A	2019 September 28		–	No (calibration failure)
FRB 20171019A	2019 October 18	$6''.8 \times 5''.0$	5.2	$<15 \mu\text{Jy beam}^{-1}$
FRB 20190711A	2019 August 23	$11''.7 \times 4''.9$	4.9	$<15 \mu\text{Jy beam}^{-1}$
FRB 20190711A	2019 September 09	$12''.5 \times 4''.9$	4.6	$<15 \mu\text{Jy beam}^{-1}$
FRB 20190714A	2019 September 14	$7''.1 \times 6''.2$	4.2	$54.4 \mu\text{Jy beam}^{-1}$
FRB 20190714A	2019 September 28	$6''.5 \times 5''.1$	5.8	$52.0 \mu\text{Jy beam}^{-1}$

In addition, we searched for signals in the ultraviolet, optical, and X-ray bands. The paper is structured as follows. In Section 2, we discuss our observations and data reduction; in Section 3, we discuss the single radio continuum detection and derived multi-wavelength upper limits. Our discussion and conclusions follow in Sections 4 and 5.

2 OBSERVATIONS AND DATA REDUCTION

2.1 MeerKAT observations

The MeerKAT 64-parabolic-dish array (Jonas & MeerKAT Team 2016; Mauch et al. 2020) is located in the Northern Karoo desert near Carnarvon, South Africa. Each ‘offset Gregorian’ parabolic dish antenna has an effective diameter of 13.5 m. The inner core of the array contains 48 of the 64 dishes in a 1 km radius, while the remaining 16 dishes are spread outward up to 8 km. The shortest and longest baselines of the MeerKAT array are 29 m and 8 km, respectively, yielding angular scales of 5 arcsec to 27 arcmin at the central frequency, of the *L*-band receiver used here, of 1283 MHz. Multi-epoch observations of the FRB fields were conducted with the MeerKAT array (Project ID: SCI-20190418-VC-01) at *L*-band (856–1712 MHz). The total integration time on-source for the FRB targets was 90 min, and a phase calibrator was observed for 2 min for every 15 min on the target FRB. J2225 – 0457, J1215 – 1731, and J1619 – 8418 were used as phase calibrators, while J1939 – 6342, J0408 – 6545 were used as bandpass and flux calibrators (observed for 5 min in the beginning and the end of the observations). Details of the MeerKAT observations are presented in Table 1. Only Stokes I (total intensity) of the MeerKAT observations are considered in this paper. The data correlation was done with the SKARAB correlator (Hickish et al. 2016) in 4k mode which gives 4096 channels across the 856 MHz bandwidth resulting in a frequency resolution of ~ 209 kHz. The data were reduced using the semi-automated MeerKAT data analysis pipelines – *oxkat*³ (Heywood 2020).

2.1.1 Imaging

The OXKAT pipeline employs a collection of publicly available radio interferometric data reduction software. The final data products, including reduced and calibrated visibility data (including self-calibration), continuum (including subband) images as well as diagnostic plots, are provided by the pipeline. The customary configuration of the OXKAT pipeline incorporates flagging, cross-calibration and self-calibration processes. In the flagging process, the low-gain bandpass edges (856–880 MHz and 1658–1800 MHz) are flagged on all baselines, along with the location of the Galactic neutral

hydrogen line at 1419.8–1421.3 MHz to exclude line contamination of the continuum imaging process. Several other radio frequency interference (RFI) prone regions of the spectrum are then flagged on baselines shorter than 600 m. Then, other possible RFI affected data are flagged out using the CASA (McMullin et al. 2007) routines RFLAG and TFCROP for the calibrators, and using the TRICOLOR package for the target fields.

The cross-calibration steps using OXKAT were standard, including setting the flux scale and deriving corrections for residual delay calibration, bandpass, and time-varying gain. The OXKAT pipeline uses the customary tasks from the CASA (McMullin et al. 2007) suite for cross-calibration. After applying all the corrections to the target field, we averaged every five channels of the data before extracting (i.e. extracting only the calibrated visibilities from the science target field) the science target. To deconvolve and image the target data, the WSClean imager (Offringa et al. 2014) was used, with the multiscale and wideband deconvolution algorithms enabled to better allow imaging of the diffuse emission present in our fields. Deconvolution was performed in ten subband images (dividing the full bandwidth into 10 chunks of subbands) of each 82 MHz wide-band (10×82 MHz). WSClean generates the multifrequency synthesis (MFS) map, in joined-channel deconvolution mode, with a central frequency of 1283 MHz. In other words, the MFS map is a full bandwidth map. In WSClean, each of the subbands is deconvolved separately with an initially high mask of $20 \sigma_{\text{rms}}$ (using the auto masking function provided by WSClean), to generate an artefact-free model of the target field for the self-calibration process. This masking threshold was iteratively reduced to a value of $3 \sigma_{\text{rms}}$ in the final iteration of imaging. The OXKAT pipeline uses the customary tasks from the Cubical software (Kenyon et al. 2018) for self-calibration. The achieved rms and synthesized beam sizes are shown in Table 1.

2.1.2 Single pulse searches

In addition to obtaining correlated data, the output data stream of the F-engine are captured, delay corrected, phased and channelized before being sent over the central beamforming network to the beamforming User Supplied Equipment (FBFUSE) that was designed and developed at the Max Planck Institute for Radio Astronomy in Bonn. For this project, FBFUSE combined the data into 764 total-intensity tied-array beams which were used to populate the primary beam of $\sim 1 \text{ deg}^2$ of the array. The data are then captured at $306.24 \mu\text{s}$ time resolution by the Transient User Supplied Equipment (TUSE), a real-time transient detection backend instrument developed by the MeerTRAP⁴ team at the University of Manchester. More details on TUSE will be presented in an upcoming paper (Stappers

³<https://ascl.net/code/v/2627>

⁴<https://www.meertrap.org/>

Table 2. Details of the radio continuum source associated with FRB 20190714A.

Field name	Observation date	Telescope	ν_{centre} (GHz)	α_{J2000}	δ_{J2000}	Maj. \times min. axis	Pos. angle	Integrated flux (μJy)
FRB 20190714A	2019 September 14	MeerKAT	1.283	12 ^h 15 ^m 55 ^s .154	−13°01′17″.30	9′.6 \times 7′.4	88.7°	93
FRB 20190714A	2019 September 28	MeerKAT	1.283	12 ^h 15 ^m 55 ^s .193	−13°01′17″.18	8′.2 \times 6′.4	12.2°	94
FRB 20190714A(N)	2021 January 13	e-MERLIN ⁷	1.510	12 ^h 15 ^m 55 ^s .116	−13°01′14″.51	0′.65 \times 0′.15	17.6°	86
FRB 20190714A(S)	2021 January 13	e-MERLIN ⁸	1.510	12 ^h 15 ^m 55 ^s .118	−13°01′16″.32	0′.64 \times 0′.26	6°	123

⁷Natural. ⁸Tapered.

et al. in preparation). The GPU-based single-pulse search pipeline AstroAccelerate⁵ (Dimoudi & Armour 2015; Adámek & Armour 2016; Adámek et al. 2017; Dimoudi et al. 2018; Adámek & Armour 2019) was used to search for bursts in real-time after incoherently de-dispersing the data in the DM range 0–5118.4 pc cm^{−3} (see Caleb et al. 2020 for more details).

2.2 e-MERLIN observations

To constrain the position of the persistent continuum emission associated with FRB 20190714A, we conducted *L*-band (centre frequency of 1.51 GHz) observations of the target with the enhanced Multi-Element Remote-Linked Interferometer Network, e-MERLIN array in the United Kingdom (project code: CY10003) on 2021 January 13 (see Section 3.1.2). Six antennas were used including the 75-m Lovell telescope and the target pointing centre was RA = 12^h15^m55^s.12, Dec. = −13°01′15″.7. The quasar J1407 + 2827 was used as the bandpass calibrator, the quasar J1331 + 3030 as the flux calibrator and the quasar J1216 − 1033 as the phase calibrator. The angular separation between the target and the phase calibrator is 2.47°. The data reduction was done following standard e-MERLIN calibration procedures⁶ with additional flagging of bad visibilities followed by imaging. We found two confusing sources in the field, at RA = 12^h15^m44^s.669, Dec. = −12°57′59″.56 and RA = 12^h15^m37^s.216, Dec. = −13°09′33″.44 at 4.1 and 9.4 arcmin from the pointing centre, respectively. They had apparent flux densities of 4 and 1.3 mJy without primary beam correction. We used these for self-calibration of the field and then subtracted them from the visibility data. We made a first image with Briggs weighting parameter robust = 1, hereafter ‘natural weighting’ (in which the visibilities are given similar weight at any position in the visibility plane) using the beam parameters as in Table 2, elongated in the Declination direction due to the low target elevation from the UK. We made a second ‘tapered’ image for which the contribution of the longest baselines was weighted down to mitigate the foreshortening of the synthesized beam (applying a Gaussian uv taper equivalent to 0′.2) by broadening the minor axis and also increasing the sensitivity to extended flux. The results of the detection of compact emission is given in Section 3.1.2.

2.3 The *Swift* satellite: UVOT and XRT observations

Neil Gehrels Swift Observatory (*Swift*) is a multiwavelength NASA space mission operating in soft-X-rays and optical/UV. Here, we use data from the X-ray Telescope (XRT) (Burrows et al. 2005) which operates in the soft X-ray domain of 0.3–10 keV as well as data taken by the UV/Optical Telescope (UVOT) (Romig et al. 2005) operating in the UV to optical domain (170–600 nm). During the

FRB 20171019A multiwavelength (MWL) observing campaign, two 2 ks target-of-opportunity (ToO) observations were performed with *Swift* from 2019-09-28 18:37:02 to 2019-09-28 21:52:54 and 2019-10-18 18:03:00 to 2019-10-18 20:03:00 on the FRB 20171019A localization region. Simultaneously with *Swift*-XRT, five UVOT images were taken with the UVM2 filter (central wavelength = 2246 Å) over the 2 epochs with a total exposure of 4 ks. The images are aspect-corrected and summed with the `uvotimsum` tool (HEASOFT 6.26). Observations were performed with *Swift*-XRT in the standard Photon Counting observing mode (PC). The XRT PC data are processed with `xrtpipeline` (HEASOFT 6.26). A summed image is extracted with `xselect`.

2.4 Very high energy gamma-ray observations with H.E.S.S.

Observations of FRB 20171019A were also obtained in the very high energy gamma-ray domain with the H.E.S.S. imaging atmospheric Cherenkov telescope array, sensitive in the range between a few tens of GeVs and 100 TeV. H.E.S.S. is located on the Khomas Highland plateau of Namibia (23°16′18″ south, 16°30′00″ east), at an elevation of ∼1800 m above sea level. Observations took place contemporaneously to the first epoch of MeerKAT observations of FRB 20171019A described above. The data set was obtained with the H.E.S.S. phase II array, including the upgraded 12 m-diameter CT1-4 telescopes (Ashton et al. 2020) and the large 28 m-diameter CT5 telescope (Bolmont et al. 2014). A standard data quality selection was applied to the data (Aharonian et al. 2006). The events have then been selected and their direction and energy reconstructed using a log-likelihood minimization comparing the recorded shower images of all triggered telescopes (requiring at least two telescopes to see the same gamma-ray event) to a semi-analytical model of air showers (de Naurois & Rolland 2009).

We define a circular region-of-interest centered on the position of FRB 20171019A with a radius of 0.12°, optimal for a point-like source of emission as expected from FRB 20171019A. The background level in this ON region was determined using the standard ‘ring background’ technique (Berge, Funk & Hinton 2007) based on a radially symmetric ring around the source position. This technique allows us to derive the background level from the same field of view and assures that the gamma-ray signal and background are estimated with the same acceptance and under the same observation conditions.

3 RESULTS

3.1 MeerKAT

The theoretical thermal noise of the MeerKAT can be calculated as

$$S_{\text{rms}} = \frac{1}{\eta_c \sqrt{n_{\text{pol}} \times N(N-1) \times \Delta\nu \times t_{\text{int}}}} \text{SEFD} \quad (1)$$

⁵<https://github.com/AstroAccelerateOrg/astro-accelerate>

⁶https://github.com/e-merlin/eMERLIN_CASA_pipeline

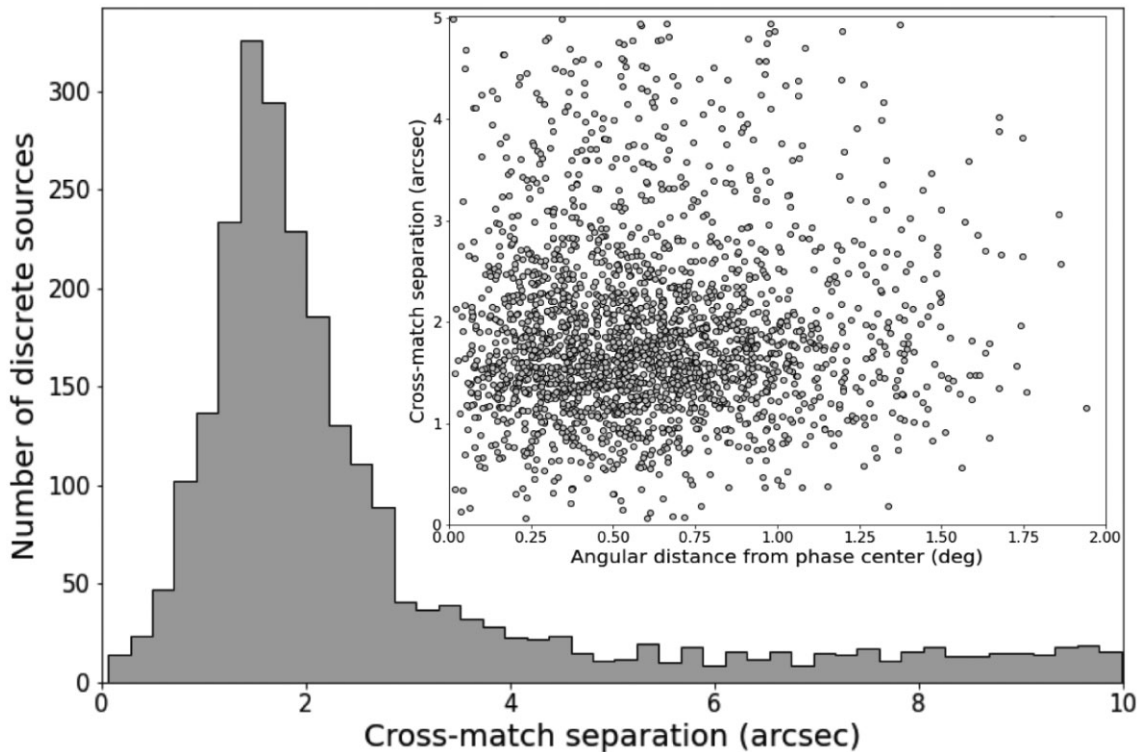


Figure 1. (top) Histogram of the cross-match separations between 2532 discrete compact sources from our MeerKAT FRB 20190714A field and *WISE* point source catalogue of the same field. The distribution of the histogram peaks at $\sim 1''.5$. (inset) A scatter plot of the angular distance from the phase center of the MeerKAT pointing against the cross-match separation up to 5 arcsec.

The system equivalent flux density (SEFD) of MeerKAT at the 1.28 GHz is 443 Jy and η_c is the correlator efficiency. We used $n_{\text{pol}} = 2$ polarization products (XX and YY), $N = 64$ telescopes, $\Delta\nu = 856$ MHz bandwidth and $t_{\text{int}} = 21600$ s observing time for one epoch. This gives the theoretical rms of $\sim 2 \mu\text{Jy beam}^{-1}$. The typical image rms obtained from our residual images is $\sim 5 \mu\text{Jy beam}^{-1}$, which is 2.5 times the expected theoretical rms. The wideband MFS image does not allow primary beam correction procedure as this can only be done on the subband images with limited rms for detection of the sources. However, our sources are at the phase centres of our fields and thus unaffected by the effect of the primary beam.

We extracted and cross-matched discrete compact (smaller in size compared to the ~ 8 arcsec synthesized beam) sources from our MeerKAT FRB 20190714A 14 September epoch with the Wide-field Infrared Survey Explorer (*WISE*) point-source catalogue. Fig. 1 (top panel) shows a histogram of the 2532 cross-match separations which peaks at $\sim 1''.5$. We found no correlation between the position uncertainty and angular distance from the phase centre of our MeerKAT observations (see Fig. 1 inset).

3.1.1 Looking for persistent continuum emission associated with the FRB fields in the MeerKAT data

Based on the results of the cross-match with *WISE* (see Fig. 1), we considered potential associations of continuum sources in the MeerKAT observations with the FRB location to sources within 5 arcsec. Using this spatial coincidence criterion, we identified a persistent 1283 MHz continuum source near FRB 20190714A, detected in both the 2019 September 14 and the 2019 September

28 epoch. The peak of the MeerKAT radio emission is offset by ~ 2.1 arcsec from the peak of the *i*-band magnitude of the optical galaxy J121555.0941 – 130116.004 identified in the Panoramic Survey Telescope and Rapid Response System (PanSTARRS, located at Haleakala Observatory) image (shown as contours in Figs 2 and 3). We identified the PanSTARRS optical source as the host of the FRB 20190714A based on their spatial coincidence. The MeerKAT radio source is offset by $1''.68$ from the localization region of FRB 20190714A (light green star in Figs 2 and 3).

3.1.2 e-MERLIN detection of compact emission towards FRB 20190714

We detect two different sources of emission in our e-MERLIN data, to the north and south of the FRB position, depending on the image weighting used:

(i) *Northern source*: Compact emission was detected in the 1.51 GHz e-MERLIN ‘natural’ image with a peak of $86 \mu\text{Jy beam}^{-1}$ at the position and beam size given in Table 2 (see light green filled circle (N) in Figs 2 and 3). The rms in this region (of full primary beam sensitivity) is $20 \mu\text{Jy}$, making this a $4.3\sigma_{\text{rms}}$ detection. Although the e-MERLIN flux scale nominal uncertainty is ~ 5 percent, in these data it is possibly higher due to the low declination of the phase-reference source and to the strong RFI which were removed from the data but may have affected the linearity of the receiver response. We conservatively adopt a flux density scale error of 10 percent. Combined with the stochastic error this gives a peak flux density uncertainty of $22 \mu\text{Jy beam}^{-1}$

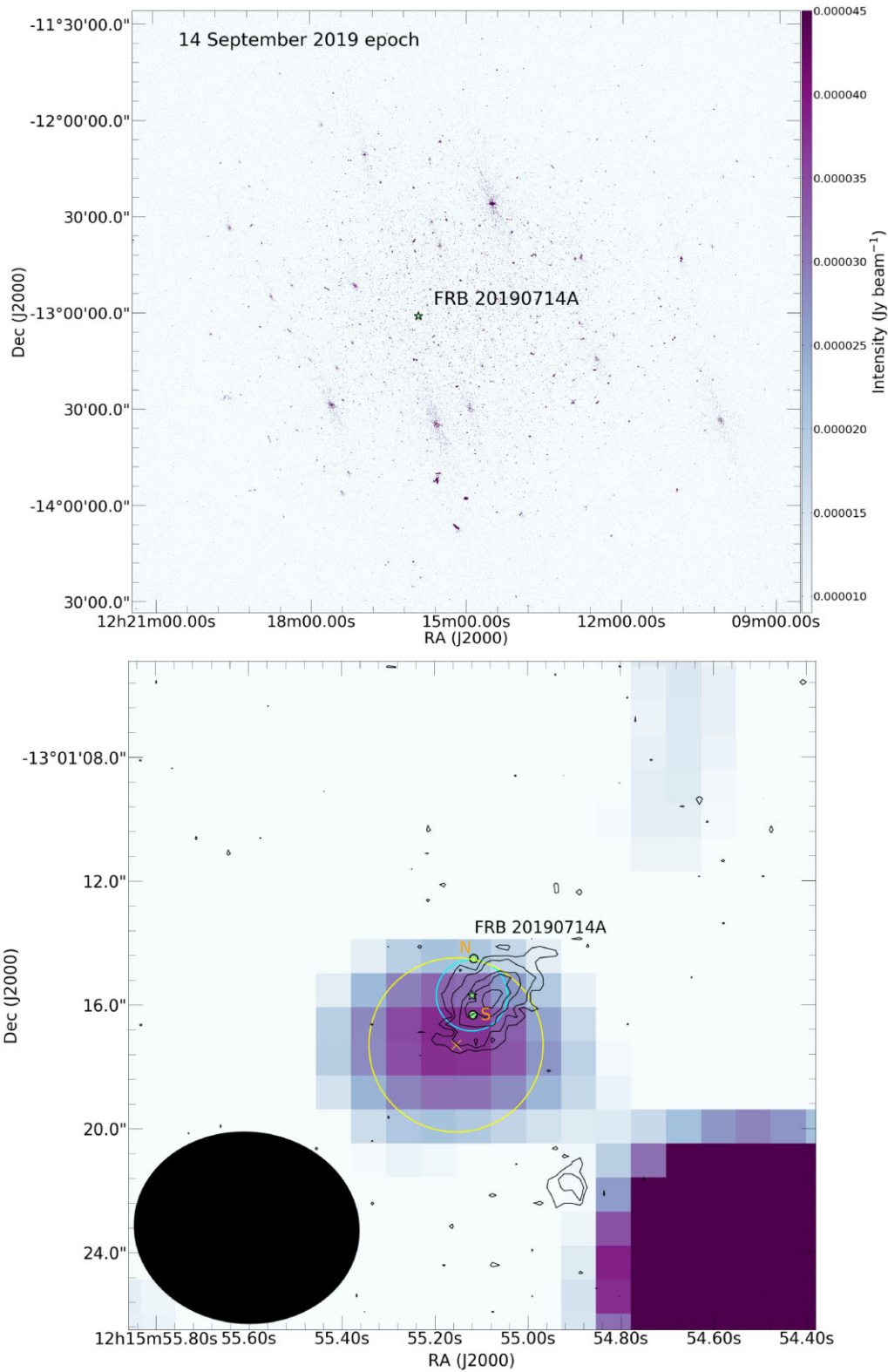


Figure 2. Top: MeerKAT image of FRB 20190714A from 2019 September 14 (bottom) and the zoom-in image centered around the position of FRB 20190714A. Contours (levels: 300, 500, 900, 1200, 1600 counts) represent the PanSTARRS *i*-band optical counterpart of the spiral galaxy coincident in position with the persistent radio emission. The black ellipse in the lower left corner represents the MeerKAT beam size. The light green star and cyan circle represent the position of the FRB and the 2σ total uncertainty in the position as determined by the ASKAP detection (Day et al. 2021). The two light green filled circles represent the peak of the two compact persistent emission (north and south indicated with orange N and S) detected with e-MERLIN. The yellow cross and yellow circle represent the peak of the MeerKAT emission and the 2σ uncertainty on the position, respectively.

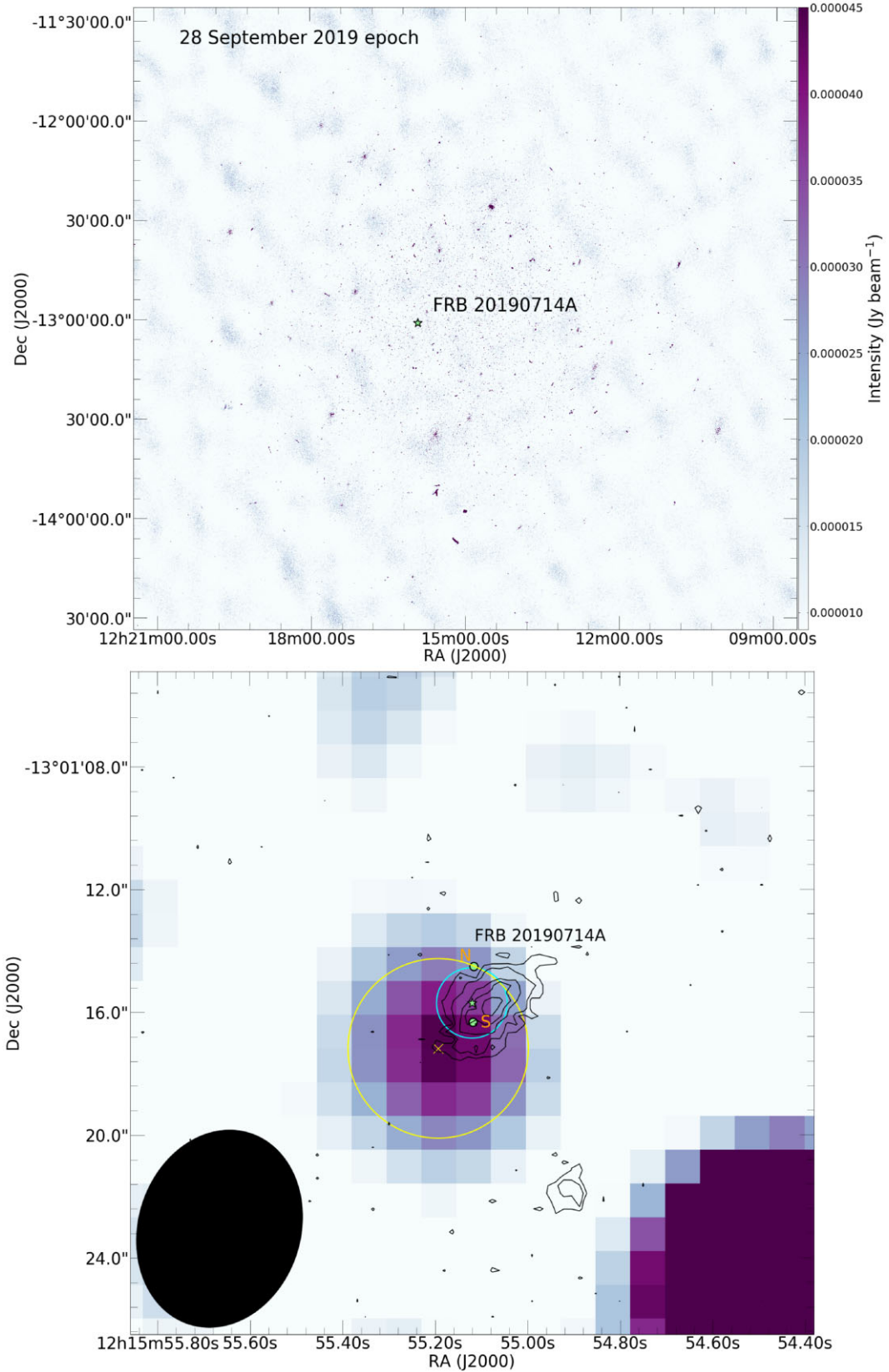


Figure 3. Top: MeerKAT image of FRB 20190714A from 2019 September 28 (bottom) and the zoom-in image centred around the position of FRB 20190714A. Contours (levels: 300, 500, 900, 1200, 1600 counts) represent the PanSTARRS *i*-band optical counterpart of the spiral galaxy coincident in position with the persistent radio emission. The black ellipse in the lower left corner represents the MeerKAT beam size. The light green star and cyan circle represent the position of the FRB and the 2σ total uncertainty in the position as determined by the ASKAP detection (Day et al. 2021). The two light green filled circles represent the peak of the two compact persistent emission (north and south indicated with orange N and S) detected with e-MERLIN. The yellow cross and yellow circle represent the peak of the MeerKAT emission and the 2σ uncertainty on the position, respectively.

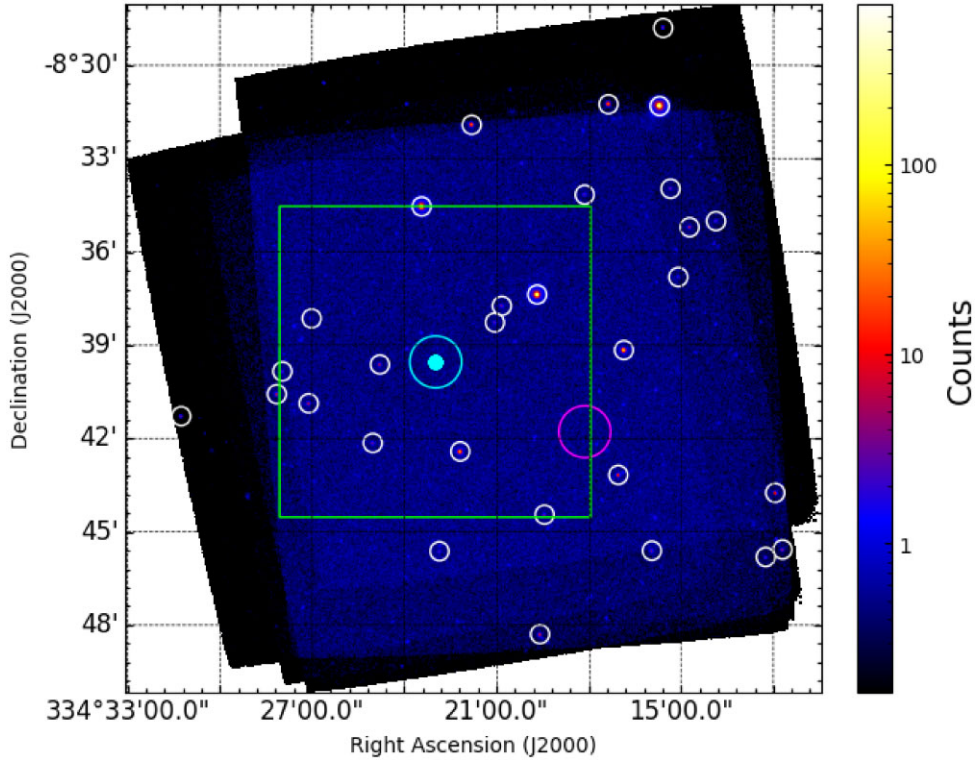


Figure 4. UVOT summed image of FRB 20171019A region taken during the MWL observation campaign in 2019 September–October. The white circles indicate sources detected above 5σ . The cyan dot denotes the location of FRB 20171019A, the circle around it indicates the region used to derive the upper limits while the magenta region indicates the background region used. The green box indicates FRB 20171019A 90 per cent localization region as reported in Kumar et al. (2019).

and integrated flux density uncertainty of $23 \mu\text{Jy}$. This makes the e-MERLIN and MeerKAT flux densities consistent at $\sim 1\sigma$ although (as discussed below and in Section 4) this may be a coincidence. This e-MERLIN source at $\text{RA} = 12^{\text{h}}15^{\text{m}}55^{\text{s}}.116$ and $\text{Dec} = -13^{\circ}01'14''.51$ is offset from the FRB position by $0''.06$ in RA and $1''.2$ in Dec. in a northerly direction. However, it is offset from the MeerKAT position by $2''.8$. The e-MERLIN stochastic position uncertainty is $(0.04, 0.16)$ arcsec and the uncertainty due to the angular and time separation between phase-calibrator and target, and antenna position errors is $(0.02, 0.07)$ arcsec. Including an allowance for residual ripples due to imperfect subtraction of confusing sources from e-MERLIN’s heterogeneous primary beams, as discussed by Muxlow et al. (2005), we estimate a total astrometric uncertainty of $(0.1, 0.25)$ arcsec in RA and Dec., respectively.

(ii) *Southern source:* A source with higher integrated flux density is revealed in the e-MERLIN ‘tapered’ image at $5.3\sigma_{\text{rms}}$ as given in Table 2, at $12^{\text{h}}15^{\text{m}}55^{\text{s}}.118 - 13^{\circ}01'16''.32$ (see light green filled circle (S) in Figs 2 and 3). This source is $0''.6$ south of the FRB position and $\sim 1''.4$ from the MeerKAT position. The total astrometric position uncertainties are $(0.2, 0.25)$ arcsec. The rms noise in the tapered image is higher, $23 \mu\text{Jy}$, and the Northern compact source discussed above is recovered but at a lower significance.

The Northern source must have an area less than 0.1 arcsec^2 (the synthesized beam), to be only detected at the higher resolution, whilst the Southern source must have a lower surface brightness but a larger area, $\sim 0.16 \text{ arcsec}^2$ above the detection threshold.

We estimate the probability of a chance alignment of a background persistent MeerKAT radio source and the host galaxy, following the procedure of Eftekhari et al. (2018). Instead of using the FRB localization region, we use the area of the galaxy, which is taken as $2 \text{ arcsec} \times 2 \text{ arcsec}$, twice the half light radius from Heintz et al. (2020). Given the source has a flux density of $\sim 90 \mu\text{Jy}$ we estimate the chance alignment probability of 0.0008, which corresponds to 3.4σ . The flux density threshold, assuming 3σ , for an unresolved radio source is $\sim 15 \mu\text{Jy}$. If instead we consider the probability of detecting any radio source above our flux density threshold of $15 \mu\text{Jy}$, the probability of a chance alignment is, therefore, approximately 0.8 per cent, making the statistical significance of our detection 2.6σ . This represents the first detection of radio continuum emission associated with the host (galaxy) of FRB 20190714A (see Figs 2 and 3). We note that ‘look-elsewhere’ effect is not taken into consideration in our chance alignment probability estimation.

3.1.3 MeerKAT non-detections

No continuum emission was detected near FRBs 20171019A and 20190711A. As each of the images of these sources has an rms of $\sim 5 \mu\text{Jy beam}^{-1}$, the 3σ intensity upper limit of any emission associated with FRBs 20171019A and 20190711A will be $\sim 15 \mu\text{Jy beam}^{-1}$ (see Table 1).

Candidate pulses above a signal-to-noise ratio (S/N) of 10 from the single-pulse search with MeerTRAP were visually inspected offline. No new FRBs or repeat bursts from the known FRBs were detected

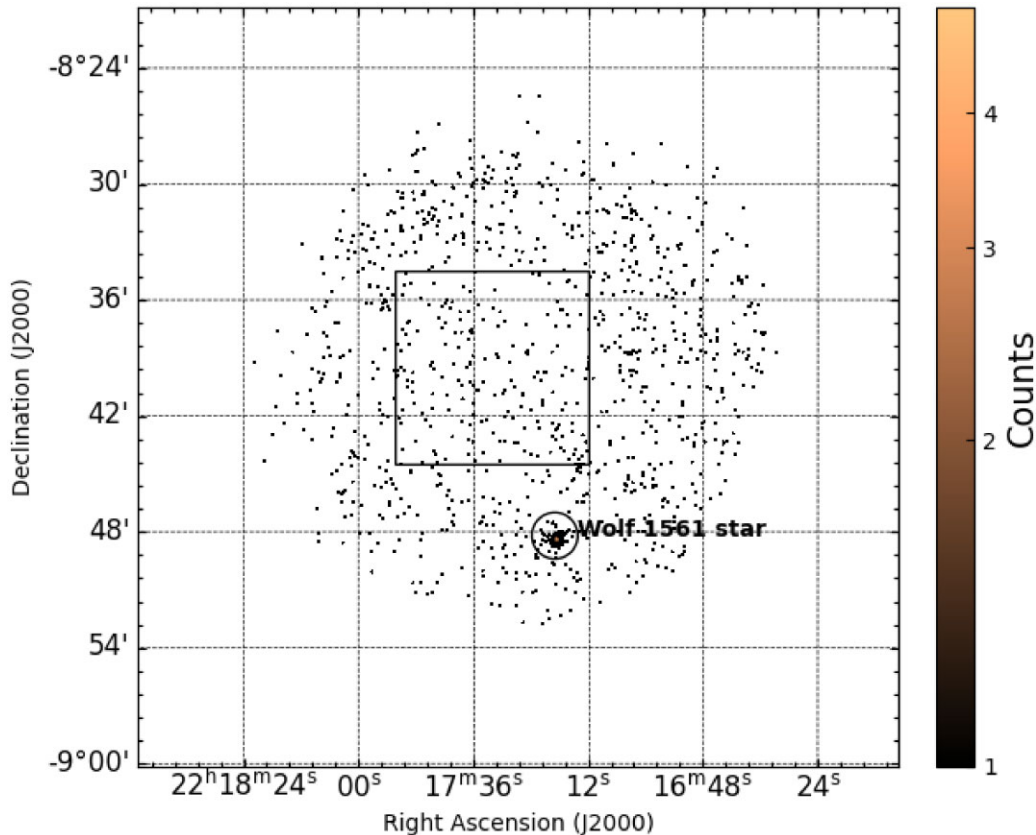


Figure 5. XRT summed image of FRB 20171019A region taken during the MWL observation campaign in 2019 September–October. The position of the Wolf 1561 star is indicated with the black open circle and labelled. The black box indicates FRB 20171019A 90 per cent localization region as reported in Kumar et al. (2019).

above a fluence threshold of 0.08 Jy ms assuming a 1 ms duration burst.

3.2 Swift

The UVOT summed image is presented in Fig. 4. The UVOT field of view corresponds roughly to the uncertainty⁹ of the localization region of FRB 20171019A (RA = 7.5 arcmin and Dec. = 7 arcmin). Using `uvotdetect`, we find 30 sources above the 5σ level and within the FRB 20171019A uncertainty region. Using a 3 arcsec maximum separation, which is slightly larger than the UVOT PSF (Breeveld et al. 2010), these sources are cross-matched with known catalogue sources. We find that out of the 30 sources detected by UVOT, 28 are spatially coincident with stars catalogued in the SDSS catalogue (DR12; Alam et al. 2015), and one source is coincident with a galaxy (AGN broad-line SDSS ID: 1237652599570890948 at $z \sim 0.156$). This galaxy is also detected by the MeerKAT radio observations.

We use the NASA/IPAC Extragalactic Database (NED)¹⁰ to search for known galaxies in the FRB 20171019A uncertainty regions. We find multiple galaxies with unknown redshifts; therefore, we cannot draw conclusions on the host galaxy from our observations.

⁹<https://www.wis-tns.org/object/20171019a>

¹⁰<https://ned.ipac.caltech.edu>; NED is funded by the National Aeronautics and Space Administration and operated by the California Institute of Technology.

Using a 50 arcsec circular ON region centred on the position of FRB 20171019A and a 50 arcsec OFF region that does not contain any of the detected sources, we run the `uvotsource` tool with a 5σ background threshold and obtain a flux upper limit of 1.4×10^{-16} erg cm⁻² s⁻¹ Å⁻¹ without applying a Galactic extinction correction.

The XRT-summed image is shown in Fig. 5. At the edge of the field of view, we detect a source spatially coincident with the Wolf 1561 star. As we consider this source unrelated to the FRB, we use the online *Swift*-XRT data products generator (Evans et al. 2007, 2009) to derive upper limits in the 0.3–10 keV range on the count rate of 0.001885 counts s⁻¹. Using `WebPIMMS`¹¹ (v4.11a) and assuming a weighted average $N_{\text{H}} = 5.12 \times 10^{20}$ cm⁻² from the direction of the source estimated from the NASA’s HEASARC¹² online tools (HI4PI Collaboration et al. 2016) and a power-law model with a photon index = 2, this upper limit translates to an energy flux of 6.6×10^{-14} erg cm⁻² s⁻¹ (8.3×10^{-14} erg cm⁻² s⁻¹ unabsorbed).

3.3 H.E.S.S.

No significant gamma-ray excess above the expected background is detected from the direction of FRB 20171019A, with 52 gamma candidate events from the source region and 524 background event. A second analysis using an independent event calibration and

¹¹<https://heasarc.gsfc.nasa.gov/cgi-bin/Tools/w3pimms/w3pimms.pl>

¹²<https://heasarc.gsfc.nasa.gov/cgi-bin/Tools/w3nh/w3nh.pl>

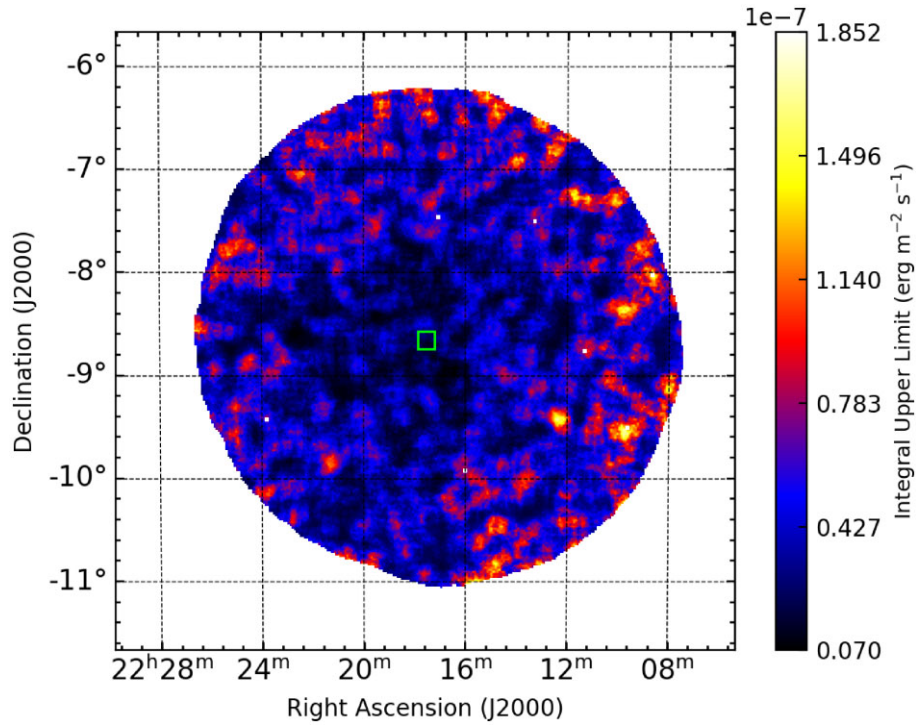


Figure 6. Map of upper limits on the VHE gamma-ray energy flux derived from the H.E.S.S. observations. The limits are valid above 120 GeV and assume a photon flux distribution following an E^{-2} dependence. The green box indicates the FRB 20171019A 90 per cent localization region as reported in Kumar et al. (2019). The oversampling radius is 0.1° .

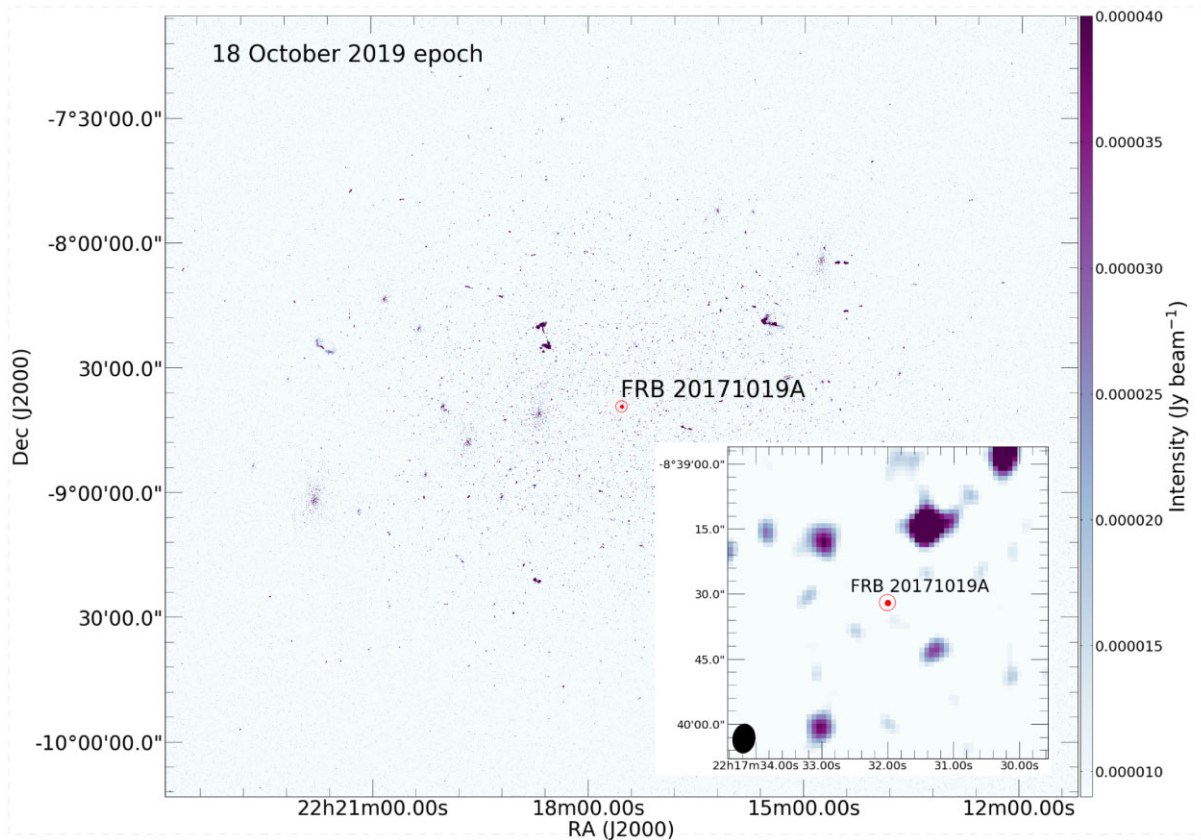


Figure 7. FRB 20171019A MeerKAT image and a zoom-in (insert) around the position of the FRB. The black ellipse on the bottom left corner of the insert represent the beam size of MeerKAT.

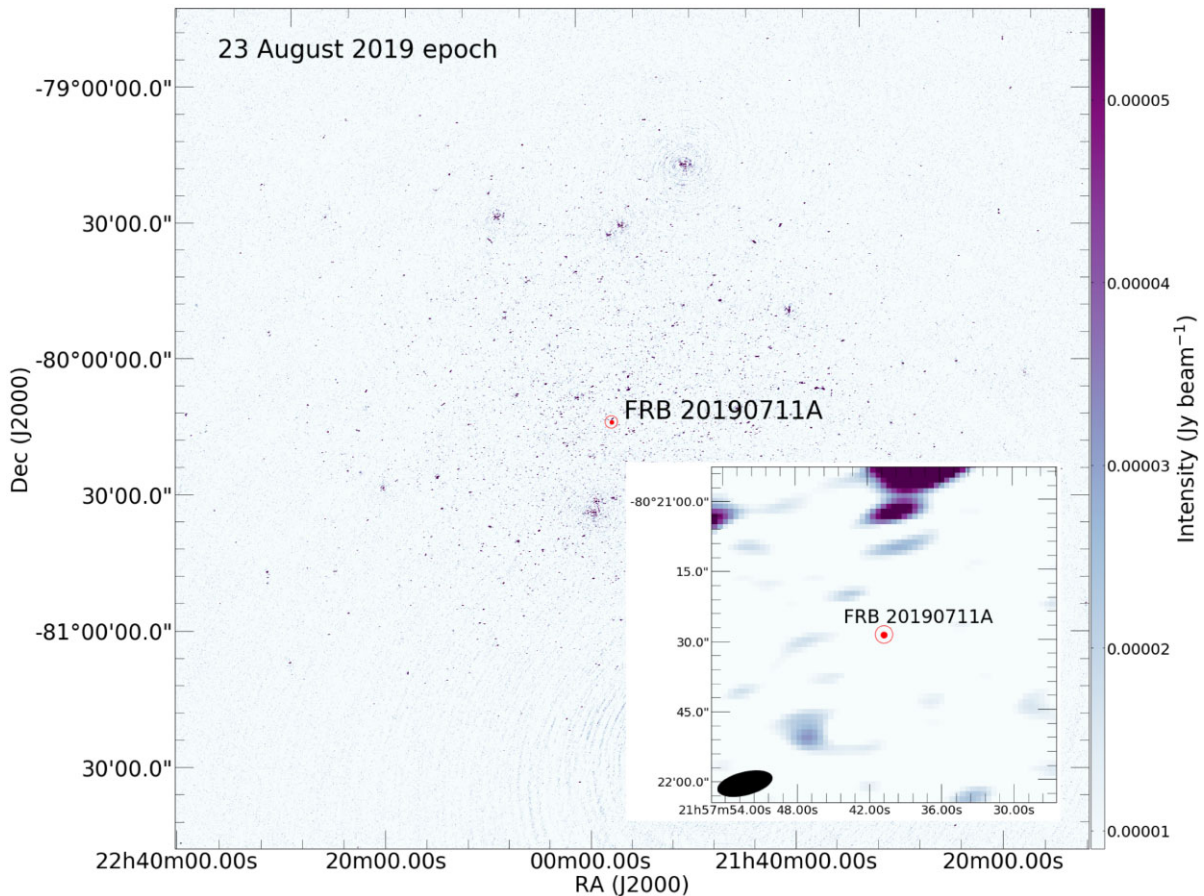


Figure 8. FRB 20190711A MeerKAT epoch I image and a zoom-in (insert) around the position of the FRB. The black ellipse on the bottom left corner of the insert represent the beam size of MeerKAT.

reconstruction (Parsons & Hinton 2014) confirms this result. A search for variable emission on time-scales ranging from milliseconds to several minutes with tools provided in Brun et al. (2020) does not reveal any variability above 2.2σ . For the total data set of 1.8 h, 95 per cent confidence level (CL) upper limits on the photon flux are derived using the method described by Rolke, López & Conrad (2005). The energy threshold of the data is highly dependent on the zenith angle of the observations. For these observations, the zenith angles range from 15 to 25 deg, which leads to an energy threshold for the stacked data set of $E_{\text{th}} = 120$ GeV. The upper limit on the Very High Energy (VHE) gamma-ray flux above that threshold and assuming an energy dependence following E^{-2} is $\Phi(E > 120 \text{ GeV}) < 2.10 \times 10^{-12} \text{ cm}^{-2} \text{ s}^{-1}$ or $\Phi(E > 120 \text{ GeV}) < 1.7 \times 10^{-12} \text{ erg cm}^{-2} \text{ s}^{-1}$. A variation of ± 0.5 of the assumed spectral index leads to a variation in the upper limit of less than ± 19 per cent. A map of energy flux upper limits covering the full region accessible within the H.E.S.S. field of view above 120 GeV is given in Fig. 6.

4 DISCUSSION

Of the targeted FRB fields reported here, only FRB 20190714A is observed to be possibly associated with a persistent radio continuum source in the MeerKAT data. We obtain an upper limit of $\sim 15 \mu\text{Jy beam}^{-1}$ for FRBs 20190711A and 20171019A, respectively, and a peak intensity of $\sim 53 \mu\text{Jy beam}^{-1}$ for the emission coincident with FRB 20190714A. This source is detected at both epochs with similar

intensities within the measured rms of the MeerKAT images (see Tables 1 and 2 for details). The values in the Table 2 are derived by carrying out 2D Gaussian fit using similar ellipses enclosing the detected persistent emission. The average flux density is ~ 3 times and ~ 4 times less than that of the persistent sources associated with two of the most prolific repeaters, FRBs 20121102A and 20190520B, respectively. Persistent radio emission from FRB 20201124A was resolved out on scales of ~ 0.1 arcsec with the European VLBI Network (Marcote et al. 2021), suggesting that it is not a compact source directly associated with the FRB. In contrast, the other localized, prolific repeating FRB 20180916A has no persistent radio counterpart.

We find that the Southern e-MERLIN source is most likely associated with the optical host galaxy/FRB. We find that the MeerKAT source is probably associated with this Southern e-MERLIN source. It should be noted that our positive chance alignment probability does not take ‘look-elsewhere’ effect into consideration. In Fig. 3 one can see that the MeerKAT persistent radio source lies at the edge of the optical extent of the host galaxy as seen in PanSTARRS observations (Heintz et al. 2020). Our derived 1283 MHz peak position with MeerKAT places it just $1'.7$ away from the position of FRB 20190714A ($\alpha_{J2000}, \delta_{J2000} = 12^{\text{h}}15^{\text{m}}55^{\text{s}}.13, -13^{\circ}01'15''.60$; Day et al. 2021). The positional uncertainty on the FRB position is $0'.4$ (Day et al. 2021). The natural e-MERLIN source North of the FRB is compact and, if the position errors are underestimated, it could be associated with the FRB but this is a very tentative possibility. The positions of the FRB and the Northern compact source are consistent

within their 2σ uncertainties. The source appearing further South in the tapered image is closer to the FRB (0'7) and the MeerKAT source (1'4). It is very likely that it and the MeerKAT source are the same (i.e. radio emission from the host galaxy), as the typical size of a fairly nearby star-forming galaxy is of order 2 arcsec, and the nominal position determined by fitting a 2D Gaussian component has an additional uncertainty as the true brightness distribution is likely to be non-Gaussian. This emission from the Galaxy itself is resolved on the longest e-Merlin baselines and so is not compact.

The Northern source detected by e-MERLIN has an upper size limit of 0.1 mas^2 but the Southern source is more extended, and thus must be larger than the very compact persistent radio source associated with FRB 20121102A (which is at a lower redshift than FRB 20190714A). We are unable to definitively state whether the Northern source is truly compact or just 0.1 mas^2 . Higher resolution imaging is required to confirm this. If the Northern source is resolved out in higher resolution images, it may be more similar to the continuum emission detected in FRB 20201124A by the uGMRT and VLA. At the angular diameter distance of FRB 20190714A (780 Mpc), an unresolved source with an angular size of $0'.6$ corresponds to a physical extent of $\lesssim 2.3 \text{ kpc}$. For 20201124A, the uGMRT reported the detection of an unresolved radio emission at 650 MHz with a flux density of $700 \pm 100 \mu\text{Jy}$ (Wharton et al. 2021), while the VLA detected persistent emission with a flux density of $340 \pm 30 \mu\text{Jy}$ at 3 GHz (Ricci et al. 2021). Assuming the estimated spectral index between these frequencies (~ -0.5 , Ricci et al. 2021), the 1.3 GHz flux density would be $\sim 500 \mu\text{Jy}$ (similar to the 3σ upper limit on observations from 1 to 2 GHz; Law et al. 2021). The flux density we measured for FRB 20190714A is a factor of ~ 10 lower than FRB 20201124A, but FRB 20190714A is also a factor of 2.6 more distant. Therefore, the flux densities would be comparable if they were at similar distances.

Given the resolution of MeerKAT, we are unable to definitively state whether the persistent emission is associated with a star-forming region or the FRB itself. The host star formation rate of $0.65 M_{\odot} \text{ yr}^{-1}$ (Heintz et al. 2020) is expected to produce a radio continuum counterpart with luminosity of $L_r \sim 10^{28} \text{ erg}^{-1} \text{ s}^{-1} \text{ Hz}^{-1}$ (Kennicutt & Evans 2012; Condon, Matthews & Broderick 2019). This is about 10 times lower than the observed radio luminosity of the source, potentially indicating a persistent radio source like that seen toward other repeating FRBs like FRB 20121102A and FRB 20190520B. However, the relations used to estimate L_r usually have an order of magnitude scatter, so new observations are required to strengthen the argument. Additionally, after accounting for the Galactic contribution to the measured FRB DM of 504.1 pc cm^{-3} , we estimate an excess DM of $\sim 460 \text{ pc cm}^{-3}$, which suggests an inferred redshift of $z \sim 0.4$ based on the Macquart relation (Macquart et al. 2020). The measured redshift of $z = 0.2365$ (Heintz et al. 2020) for the spiral host galaxy suggests that a significant contribution of $\sim 180 \text{ pc cm}^{-3}$ must either be accounted for by the host galaxy itself, an intervening foreground galaxy or cosmic structure along the line of sight. Interestingly, both repeating FRBs 20121102A and 20190520, which are associated with persistent radio emission, also have significant DM excesses arising from their respective host galaxies (Tendulkar et al. 2017b; Niu et al. 2022).

One of the leading models to explain the bursts from, and radio counterpart to FRB 20121102A, is a young, nebula powered flaring magnetar embedded in a 20–50-yr-old supernova remnant (Beloborodov 2017; Metzger, Margalit & Sironi 2019). The lack of a bright persistent radio source associated with the repeater FRB 20180916A suggests that it is comparatively older at $\gtrsim 200$ –500 yr and the persistent radio source may have faded. In the model

by Metzger et al. (2019), the nebula is suggested to contribute significantly to the rotation measure and dispersion measure (DM), as well as to the persistent radio luminosity. These values are expected to decrease on a time-scale of a few decades to centuries. Given the association of a comparatively fainter persistent source, FRB 20190714A may potentially be a repeating FRB whose age lies between that of FRB 20121102A and FRB 20180916A. Millisecond magnetars formed through standard astrophysical channels such as hydrogen poor superluminous supernovae and long-duration gamma-ray bursts are consistent with the progenitors of FRBs expected in low-metallicity dwarf galaxies with high specific star formation rate such as for FRB 20121102A. However, Margalit et al. (2019) note that it is also possible to form such sources through a variety of channels, including binary neutron star mergers and accretion-induced collapse of white dwarfs in environments and host galaxy demographics different to FRB 20121102A. Such suggestions are consistent with recent localizations (e.g. Heintz et al. 2020; Bhandari et al. 2022).

The X-ray and VHE observations with *Swift* and H.E.S.S. allows us to probe non-thermal persistent emission associated to the FRB host galaxy or its source. Recently, H.E.S.S. observed SGR1935 + 2154 (H.E.S.S. collaboration 2021) that is a Galactic magnetar linked to a repeating FRB and its first X-ray counterpart. Magnetar X-ray flares could in fact be non-thermal in nature (Li et al. 2021) indicating the presence of particle acceleration that could potentially reach the VHE domain. The inverse Compton process is a primary candidate for the production of VHE non-thermal emission. H.E.S.S. observations did not lead to a detection of a persistent or a transient source associated to FRB 20171019A. We found no X-ray counterparts and thus derived the upper limits to constrain these emissions. In the case of existence of X-ray non-thermal outbursts, the lack of VHE detection could hypothetically indicate that inverse Compton is weak in the vicinity of the magnetars or that the VHE gamma-ray emission is quenched. This latter scenario could be explained by the fact that inverse Compton is taking place too close to the magnetar's surface, where pair production and photon splitting could be responsible for significant energy losses (Hu et al. 2019), preventing energetic particles and photons to reach the nebula.

No persistent emissions were detected towards FRB 20190711A and FRB 20171019A in our MeerKAT observations (see Figs 7–9), therefore no follow-up observations were conducted towards those FRBs.

5 CONCLUSIONS

Several FRB models envision persistent emission to be associated with these sources. In this paper, we conducted radio observations of three FRBs (FRB 20190714A, 20190711A, and 20171019A), and also a multiwavelength campaign on one of these (FRB 20171019A).

We detected possible persistent compact radio emission associated with FRB 20190714A (at $z = 0.2365$) using the MeerKAT and e-MERLIN radio telescopes. We are unable to definitively claim the association of the compact source with the FRB with the current data. The low detection significance of the compact source makes it possible for it to be a spurious detection. Given the noisy environment of e-MERLIN and the highly elongated synthesized beam at the declination of the FRB, it is also likely that the e-MERLIN position errors might be underestimated, if the source is indeed real. Higher resolution imaging is necessary to remove any ambiguities and provide certainty about the size and location of the continuum radio emission. If confirmed, this could represent the first detection of the radio continuum emission associated with the host (galaxy) of FRB

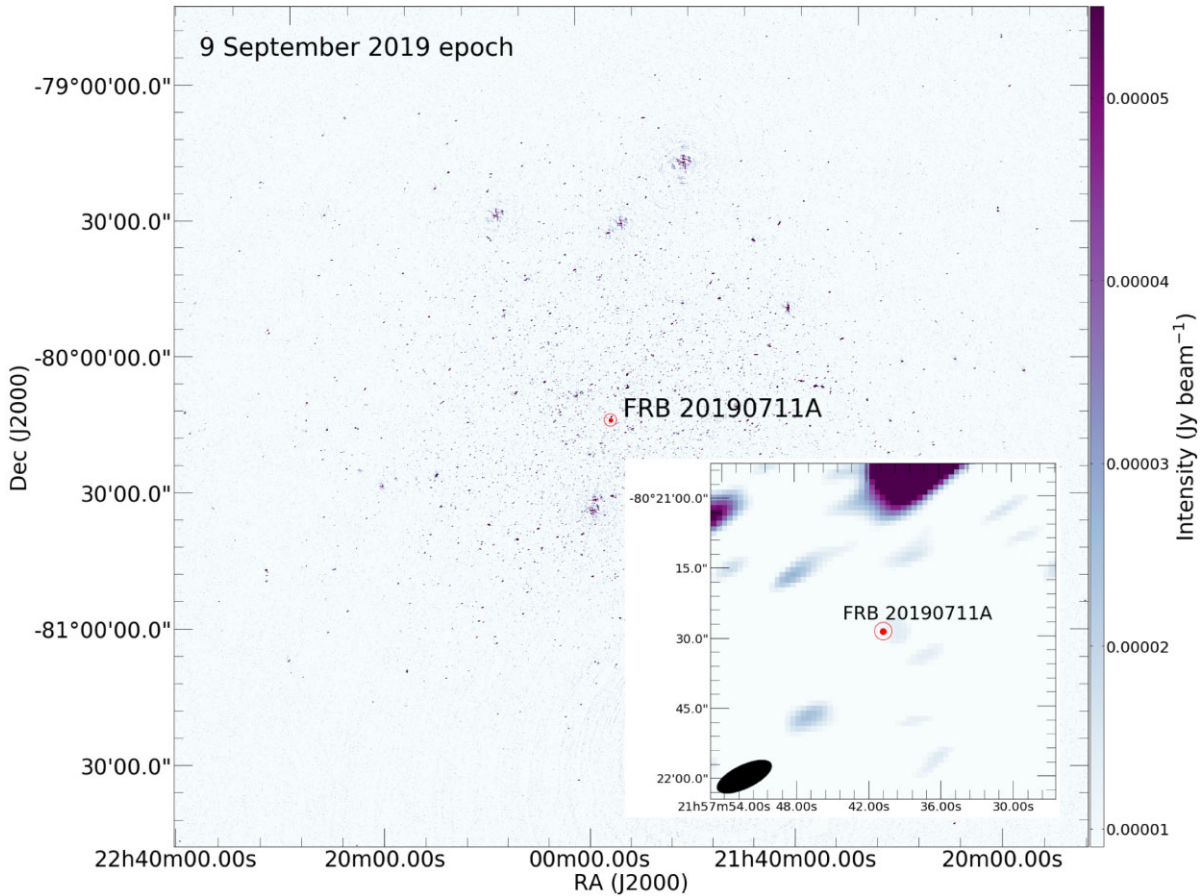


Figure 9. FRB 20190711A MeerKAT epoch II image and a zoom-in (insert) around the position of the FRB. The black ellipse on the bottom left corner of the insert represent the beam size of MeerKAT.

20190714A. Additionally, it would suggest that all FRBs, repeaters and non-repeaters alike, originate from similar emission processes with a combination of effects governing their repetition rates, spectral properties and local environments. We also performed UV, X-ray, and VHE observations with the *Swift* and H.E.S.S. instruments and obtained upper limits in the three domains constraining the MWL emissions from FRB 20171019A. The search for FRB MWL counterparts is ongoing within the H.E.S.S. collaboration and more results will be published in future works.

We furthermore obtained a radio upper limit of $\sim 15 \mu\text{Jy beam}^{-1}$ for the repeating FRBs 20190711A and 20171019A.

ACKNOWLEDGEMENTS

This paper makes use of the MeerKAT data (Project ID: SCI-20190418-VC-01). The MeerKAT telescope is operated by the South African Radio Astronomy Observatory, which is a facility of the National Research Foundation, an agency of the Department of Science and Innovation (DSI). This work made use of the Inter-University Institute for Data Intensive Astronomy (IDIA) visualization lab <https://vislab.idia.ac.za>. IDIA is a partnership of the University of Cape Town, the University of Pretoria, the University of the Western Cape and the South African Radio astronomy Observatory. e-MERLIN is a National Facility operated by the University of Manchester at Jodrell Bank Observatory on behalf of STFC. The authors would like to acknowledge the use of the Centre for High-Performance Computing resources in South Africa in this work.

The authors acknowledge funding from the European Research Council (ERC) under the European Union's Horizon 2020 research and innovation programme (grant agreement No 694745). The support of the Namibian authorities and of the University of Namibia in facilitating the construction and operation of H.E.S.S. is gratefully acknowledged, as is the support by the German Ministry for Education and Research (BMBF), the Max Planck Society, the German Research Foundation (DFG), the Helmholtz Association, the Alexander von Humboldt Foundation, the French Ministry of Higher Education, Research and Innovation, the Centre National de la Recherche Scientifique (CNRS/IN2P3 and CNRS/INSU), the Commissariat à l'énergie atomique et aux énergies alternatives (CEA), the U.K. Science and Technology Facilities Council (STFC), the Knut and Alice Wallenberg Foundation, the National Science Centre, Poland grant no. 2016/22/M/ST9/00382, the South African Department of Science and Technology and National Research Foundation, the University of Namibia, the National Commission on Research, Science & Technology of Namibia (NCRST), the Austrian Federal Ministry of Education, Science and Research and the Austrian Science Fund (FWF), the Australian Research Council (ARC), the Japan Society for the Promotion of Science and by the University of Amsterdam. We appreciate the excellent work of the technical support staff in Berlin, Zeuthen, Heidelberg, Palaiseau, Paris, Saclay, Tübingen and in Namibia in the construction and operation of the equipment. This work benefited from services provided by the H.E.S.S. Virtual Organization, supported by the national resource providers of the EGI Federation.

DATA AVAILABILITY

The data underlying this article will be shared on reasonable request to the corresponding authors.

REFERENCES

- Abdalla H. et al., 2021, *ApJ*, 919, 106
- Adámek K., Armour W., 2016, preprint ([arXiv:1611.09704](https://arxiv.org/abs/1611.09704))
- Adámek K., Armour W., 2019, *ASPC*, 523, 489
- Adámek K., Dimoudi S., Giles M., Armour W., 2017, preprint ([arXiv:1711.10855](https://arxiv.org/abs/1711.10855))
- Aharonian F. et al., 2006, *A&A*, 457, 899
- Alam S. et al., 2015, *ApJS*, 219, 12
- Ashton T. et al., 2020, *Astroparticle Physics*, 118, 102425
- Bannister K. W. et al., 2019, *Science*, 365, 565
- Bassa C. G. et al., 2017, *ApJ*, 843, L8
- Beloborodov A. M., 2017, *ApJ*, 843, L26
- Berge D., Funk S., Hinton J., 2007, *A&A*, 466, 1219
- Bhandari S. et al., 2020, *ApJ*, 895, L37
- Bhandari S. et al., 2022, *AJ*, 163, 69
- Bolmont J. et al., 2014, *NIMA*, 761, 46
- Breeveld A. A. et al., 2010, *MNRAS*, 406, 1687
- Brun F., Piel Q., de Naurois M., Bernhard S., 2020, *Astropart. Phys.*, 118, 102429
- Burrows D. N. et al., 2005, *Space Sci. Rev.*, 120, 165
- Caleb M. et al., 2020, *MNRAS*, 496, 4565
- Caleb M., Keane E., 2021, *Universe*, 7, 453
- Caleb M., Stappers B. W., Rajwade K., Flynn C., 2019, *MNRAS*, 484, 5500
- Chatterjee S. et al., 2017, *Nature*, 541, 58
- Chime/FRB Collaboration, 2021, *Astron. Tel.*, 14497, 1
- Condon J. J., Matthews A. M., Broderick J. J., 2019, *ApJ*, 872, 148
- Cordes J. M., Wasserman L., 2016, *MNRAS*, 457, 232
- Dai Z. G., Wang J. S., Yu Y. W., 2017, *ApJ*, 838, L7
- Day C. K., Deller A. T., James C. W., Lenc E., Bhandari S., Shannon R. M., Bannister K. W., 2021, *PASA*, 38, e050
- de Naurois M., Rolland L., 2009, *Astropart. Phys.*, 32, 231
- Dimoudi S., Adamek K., Thiagaraj P., Ransom S. M., Karastergiou A., Armour W., 2018, *ApJS*, 239, 28
- Dimoudi S., Armour W., 2015, preprint ([arXiv:1511.07343](https://arxiv.org/abs/1511.07343))
- Eftekhari T., Berger E., Williams P. K. G., Blanchard P. K., 2018, *ApJ*, 860, 73
- Evans P. A. et al., 2007, *A&A*, 469, 379
- Evans P. A. et al., 2009, *MNRAS*, 397, 1177
- Fong W.-F. et al., 2021, *ApJ*, 919, L23
- Heintz K. E. et al., 2020, *ApJ*, 903, 152
- Heywood I., 2020, *oxkat*: Semi-automated imaging of MeerKAT observations ([ascl:2009.003](https://ascl.net/2009.003))
- HI4PI Collaboration et al., 2016, *A&A*, 594, A116
- Hickish J. et al., 2016, *J. Astron. Instr.*, 5, 1641001
- Hilmarsson G. H. et al., 2021, *ApJ*, 908, L10
- Hu K., Baring M. G., Wadiasingh Z., Harding A. K., 2019, *MNRAS*, 486, 3327
- Insight-HXMT, 2020, SGR J1935 + 2154 burst list, <http://hxmtcn.ihep.ac.cn/bfy/331.jhtml>
- James C. W. et al., 2020, *MNRAS*, 495, 2416
- Jonas J., MeerKAT Team, 2016, in *MeerKAT Science: On the Pathway to the SKA*. p. 1
- Kashiyama K., Ioka K., Mészáros P., 2013, *ApJ*, 776, L39
- Kennicutt R. C., Evans N. J., 2012, *ARA&A*, 50, 531
- Kenyon J. S., Smirnov O. M., Grobler T. L., Perkins S. J., 2018, *MNRAS*, 478, 2399
- Kumar P. et al., 2019, *ApJ*, 887, L30
- Kumar P. et al., 2021, *MNRAS*, 500, 2525
- Law C. J., Connor L., Aggarwal K., 2022, *ApJ*, 927, 55
- Law C., Tendulkar S., Clarke T., Aggarwal K., Bethapudy S., 2021, *Astron. Tel.*, 14526, 1
- Li C. K. et al., 2021, *Nat. Astron.*, 5, 378
- Liu T., Romero G. E., Liu M.-L., Li A., 2016, *ApJ*, 826, 82
- Lorimer D. R., Bailes M., McLaughlin M. A., Narkevic D. J., Crawford F., 2007, *Science*, 318, 777
- Lyubarsky Y., 2014, *MNRAS: Lett*, 442, L9
- Macquart J. P. et al., 2020, *Nature*, 581, 391
- Marcote B. et al., 2017, *ApJ*, 834, L8
- Marcote B. et al., 2020, *Nature*, 577, 190
- Marcote B. et al., 2021, *Astron. Tel.*, 14603, 1
- Margalit B., Berger E., Metzger B. D., 2019, *ApJ*, 886, 110
- Mauch T. et al., 2020, *ApJ*, 888, 61
- McMullin J. P., Waters B., Schiebel D., Young W., Golap K., 2007, in Shaw R. A., Hill F., Bell D. J., eds, *ASP Conf. Ser. Vol. 376, Astronomical Data Analysis Software and Systems XVI*. *Astron. Soc. Pac.*, San Francisco, p. 127
- Mereghetti S. et al., 2020, *ApJ*, 898, L29
- Metzger B. D., Berger E., Margalit B., 2017, *ApJ*, 841, 14
- Metzger B. D., Margalit B., Sironi L., 2019, *MNRAS*, 485, 4091
- Muxlow T. W. B. et al., 2005, *MNRAS*, 358, 1159
- Niu C. H. et al., 2022, *Nature*, 606, 873
- Offringa A. R. et al., 2014, *MNRAS*, 444, 606
- Parsons R. D., Hinton J. A., 2014, *Astropart. Phys.*, 56, 26
- Petroff E., Hessels J. W. T., Lorimer D. R., 2022, *Astron. Astrophys. Rev.*, 30, 2
- Platts E., Weltman A., Walters A., Tendulkar S. P., Gordin J. E. B., Kandhai S., 2019, *Phys. Rep.*, 821, 1
- Popov S. B., Postnov K. A., 2013, preprint ([arXiv:1307.4924](https://arxiv.org/abs/1307.4924))
- Popov S. B., Pshirkov M. S., 2016, *MNRAS*, 462, L16
- Popov S., Postnov K., Pshirkov M., 2018, *Int. J. Mod. Phys. D*, 27, 1844016
- Prochaska J. X. et al., 2019, *Science*, 366, 231
- Ravi V. et al., 2022, *MNRAS*, 513, 982
- Ravi V., 2019, *Nat. Astron.*, 3, 928
- Resmi L., Vink J., Ishwara-Chandra C. H., 2021, *A&A*, 655, A102
- Ricci R., Piro L., Panessa F., O'Connor B., Lotti S., Bruni G., Zhang B., 2021, *Astron. Tel.*, 14549, 1
- Ridnaia A. et al., 2021, *Nat. Astron.*, 5, 372
- Rolke W. A., López A. M., Conrad J., 2005, *Nucl. Instr. Methods Phys. Res. A*, 551, 493
- Roming P. W. A. et al., 2005, *Space Sci. Rev.*, 120, 95
- Tavani M. et al., 2021, *Nature Astron.*, 5, 401
- Tendulkar S. P. et al., 2017a, *ApJ*, 834, L7
- Tendulkar S. P. et al., 2017b, *ApJ*, 834, L7
- Thornton D. et al., 2013, *Science*, 341, 53
- Totani T., 2013, *PASJ*, 65, L12
- Vieyro F. L., Romero G. E., Bosch-Ramon V., Marcote B., del Valle M. V., 2017, *A&A*, 602, A64
- Wharton R. et al., 2021, *Astron. Tel.*, 14529, 1
- Yamasaki S., Totani T., Kiuchi K., 2018, *PASJ*, 70, 39
- Zhang B., 2018, *ApJ*, 854, L21

¹Centre for Space Research, North-West University, Potchefstroom 2531, South Africa

²Department of Physics and Astronomy, Faculty of Physical Sciences, University of Nigeria, Carver Building, 1 University Road, Nsukka 410001, Nigeria

³Jodrell Bank Centre for Astrophysics, Department of Physics and Astronomy, University of Manchester, Manchester M13 9PL, UK

⁴Sydney Institute for Astronomy, School of Physics, The University of Sydney, NSW 2006, Australia

⁵Max-Planck-Institut für Radioastronomie, Auf dem Hügel 69, D-53121 Bonn, Germany

⁶IRFU, CEA, Université Paris-Saclay, F-91191 Gif-sur-Yvette, France

⁷Laboratoire Leprince-Ringuet, École Polytechnique, CNRS, Institut Polytechnique de Paris, F-91128 Palaiseau, France

⁸Department of Physics and Electronics, Rhodes University, PO Box 94, Grahamstown 6140, South Africa

⁹South African Radio Astronomy Observatory, Black River Park, 2 Fir Street, Observatory, Cape Town 7925, South Africa

- ¹⁰*Astrophysics, Department of Physics, University of Oxford, Keble Road, Oxford OX1 3RH, UK*
- ¹¹*CSIRO, Space and Astronomy, PO Box 1130, Bentley, WA 6102, Australia*
- ¹²*National University of Ireland Galway, University Road, Galway H91 TK33, Ireland*
- ¹³*SKA Observatory, Jodrell Bank Observatory, Macclesfield, Cheshire SK11 9DL, UK*
- ¹⁴*Dublin Institute for Advanced Studies, 31 Fitzwilliam Place, Dublin 2, Ireland*
- ¹⁵*Max-Planck-Institut für Kernphysik, P.O. Box 103980, D-69029 Heidelberg, Germany*
- ¹⁶*High Energy Astrophysics Laboratory, RAU, 123 Hovsep Emin St Yerevan 0051, Armenia*
- ¹⁷*Landessternwarte, Universität Heidelberg, Königstuhl, D-69117 Heidelberg, Germany*
- ¹⁸*Aix Marseille Université, CNRS/IN2P3, CPPM, 13009, Marseille, France*
- ¹⁹*University of Namibia, Department of Physics, Private Bag 13301, Windhoek 10005, Namibia*
- ²⁰*Instytut Fizyki Jądrowej PAN, ul. Radzikowskiego 152, 31-342 Kraków, Poland*
- ²¹*DESY, D-15738 Zeuthen, Germany*
- ²²*School of Physics, University of the Witwatersrand, 1 Jan Smuts Avenue, Braamfontein, Johannesburg, 2050 South Africa*
- ²³*Université de Paris, CNRS, Astroparticule et Cosmologie, F-75013 Paris, France*
- ²⁴*Department of Physics and Electrical Engineering, Linnaeus University, 351 95 Växjö, Sweden*
- ²⁵*Laboratoire Univers et Théories, Observatoire de Paris, Université PSL, CNRS, Université de Paris, F-92190 Meudon, France*
- ²⁶*Sorbonne Université, Université Paris Diderot, Sorbonne Paris Cité, CNRS/IN2P3, Laboratoire de Physique Nucléaire et de Hautes Energies, LPNHE, 4 Place Jussieu, F-75252 Paris, France*
- ²⁷*Université Savoie Mont Blanc, CNRS, Laboratoire d'Annecy de Physique des Particules - IN2P3, F-74000 Annecy, France*
- ²⁸*Astronomical Observatory, The University of Warsaw, Al. Ujazdowskie 4, PL-00-478 Warsaw, Poland*
- ²⁹*Friedrich-Alexander-Universität Erlangen-Nürnberg, Erlangen Centre for Astroparticle Physics, Erwin-Rommel-Str. 1, D-91058 Erlangen, Germany*
- ³⁰*University of Oxford, Department of Physics, Denys Wilkinson Building, Keble Road, Oxford OX1 3RH, UK*
- ³¹*Université Bordeaux, CNRS/IN2P3, Centre d'Études Nucléaires de Bordeaux Gradignan, F-33175 Gradignan, France*
- ³²*Institut für Physik und Astronomie, Universität Potsdam, Karl-Liebknecht-Strasse 24/25, D-14476 Potsdam, Germany*
- ³³*Obserwatorium Astronomiczne, Uniwersytet Jagielloński, ul. Orła 171, PL-30-244 Kraków, Poland*
- ³⁴*Institute of Astronomy, Faculty of Physics, Astronomy and Informatics, Nicolaus Copernicus University, Grudziadzka 5, PL-87-100 Torun, Poland*
- ³⁵*Nicolaus Copernicus Astronomical Center, Polish Academy of Sciences, ul. Bartycka 18, PL-00-716 Warsaw, Poland*
- ³⁶*Institut für Astronomie und Astrophysik, Universität Tübingen, Sand 1, D-72076 Tübingen, Germany*
- ³⁷*Institut für Physik, Humboldt-Universität zu Berlin, Newtonstr. 15, D-12489 Berlin, Germany*
- ³⁸*Laboratoire Univers et Particules de Montpellier, Université Montpellier, CNRS/IN2P3, CC 72, Place Eugène Bataillon, F-34095 Montpellier Cedex 5, France*
- ³⁹*Institut für Astro- und Teilchenphysik, Leopold-Franzens-Universität Innsbruck, A-6020 Innsbruck, Austria*
- ⁴⁰*Department of Physics and Astronomy, The University of Leicester, University Road, Leicester LE1 7RH, UK*
- ⁴¹*GRAPPA, Anton Pannekoek Institute for Astronomy, University of Amsterdam, Science Park 904, NL-1098 XH Amsterdam, the Netherlands*
- ⁴²*School of Physical Sciences, University of Adelaide, Adelaide 5005, Australia*
- ⁴³*Yerevan Physics Institute, 2 Alikhanian Brothers St., 375036 Yerevan, Armenia*
- ⁴⁴*Kavli Institute for the Physics and Mathematics of the Universe (WPI), The University of Tokyo Institutes for Advanced Study (UTIAS), The University of Tokyo, 5-1-5 Kashiwa-no-Ha, Kashiwa, Chiba, 277-8583, Japan*
- ⁴⁵*Department of Physics, Konan University, 8-9-1 Okamoto, Higashinada, Kobe, Hyogo 658-8501, Japan*
- ⁴⁶*RIKEN, 2-1 Hirosawa, Wako, Saitama 351-0198, Japan*

This paper has been typeset from a $\text{\TeX}/\text{\LaTeX}$ file prepared by the author.